

DIPARTIMENTO DI MATEMATICA
“Francesco Brioschi”
POLITECNICO DI MILANO

**Multiscale Modeling and Simulation
of Organic Solar Cells**

de Falco, C.; Porro, M.; Sacco, R.; Verri, M.

Collezione dei *Quaderni di Dipartimento*, numero **QDD 93**
Inserito negli *Archivi Digitali di Dipartimento* in data 11-4-2011



Piazza Leonardo da Vinci, 32 - 20133 Milano (Italy)

Multiscale Modeling and Simulation of Organic Solar Cells

Carlo de Falco^{a,b}, Matteo Porro^c, Riccardo Sacco^a, Maurizio Verri^a

^a*Dipartimento di Matematica “F.Brioschi”, Politecnico di Milano,
Piazza L. da Vinci 32, 20133 Milano Italy*

^b*MOX Modeling and Scientific Computing*

^c*Center for Nanoscience and Technology of IIT@PoliMi
via Pascoli 70/3, Milano 20133 Italy*

Abstract

In this article, we continue our mathematical study of organic photovoltaic device models started off in [12] focusing on the issue of accurately modeling the impact of the interface morphology on device performance. To this end, we propose a multi-dimensional model for bilayer organic solar cell devices with arbitrary interface geometries derived by averaging the mass balance equations across the interface thickness. This yields a system of incompletely parabolic nonlinear PDEs to describe mass transport in the materials, coupled with ODEs localized at the heterojunction. We perform the numerical approximation of the differential system in stationary conditions and we apply it to the simulation of a variety of devices with different morphologies.

Keywords: Organic photovoltaic devices; solar cells; reaction-diffusion systems with electrostatic convection; numerical simulation; finite element method.

1. Introduction and Motivation

Research on photovoltaic energy conversion has recently received great impulse due to the growing demand for low carbon dioxide emission energy sources. In particular, the high manufacturing cost of crystalline silicon and the latest advancements on semiconducting polymer design and synthesis in recent years have directed the attention of the scientific community towards Organic Solar Cells (OSCs), *i.e.* solar cells based on organic materials [8, 15, 16, 26, 27, 29, 31], especially because of the very limited thermal budget required for the production of such materials and of their amenability to be deposited on large areas, which is fundamental in light harvesting applications.

One of the main peculiarities of OSCs is that most physical phenomena that are critical for charge photogeneration occur at the interface between the two materials that constitute the active layer of such devices. In order to increase cell efficiencies, currently of the order of about 8% [22, 17], the optimization of the morphology of such interface is considered by device designers to be an issue at

least as important as the optimization of the donor and acceptor optoelectronic characteristics.

For this reason, in this article we continue our mathematical study of organic photovoltaic device models started off in [12] focusing on the issue of accurately modeling the impact of the interface morphology on device performance. To this end, we present an extension of the one-dimensional model for bilayer OSC devices proposed in [3] to the case of arbitrary interface geometries.

Compared to previously proposed multidimensional models [6, 33, 20], our approach is characterized by a systematic use of the average across the interface thickness of the mass balance system equations. This amounts to “lumping” the equations describing the interface phenomena into suitable flux transmission conditions. The multiscale perspective of the proposed formulation is similar to model-reduction techniques used in porous media with thin fractures [25] and has the advantage of simplifying the discrete computational domain while allowing, at the same time, to easily include in the model a local dependency of the coefficients on the orientation of the electric field.

The present paper is structured as follows. In Section 2 we start by briefly describing the sequence of physical phenomena that lead from photon absorption to current harvesting in an OSC. In Section 3 we present the system of equations to model charge generation and transport, initially considering an interface of finite thickness (Section 3.2), and then deducing simplified transmission conditions to be enforced at the material separation interface (Section 3.3). Section 4 details the numerical methods adopted for the solution of the model equations, while Section 5 is devoted to presenting and discussing some simulation results. Finally, in Section 6 we draw some conclusions and sketch possible directions to be followed in further research on this topic.

2. Basic Principles of Photocurrent Generation in OSCs

In this section, we describe the basic principles of photocurrent generation in OSCs only to the extent strictly needed for understanding the naming conventions adopted in the following sections. For a more thorough introduction to the subject, we refer the interested reader to [15, 29, 26].

A schematic representation of the typical structure of an OSC is shown in Fig. 1. The photoactive layer of the device consists of two materials, one with higher electron affinity (the “acceptor”, for example F8BT) and one with lower electron affinity (the “donor”, for example PFB), sandwiched between two electrodes, one of which is transparent to allow light to enter the photoactive layer while the other is reflecting in order to increase the light path through the device.

The sequence of physical phenomena that leads from photon absorption to current harvesting at the device contacts is represented in Fig. 2.

Absorption of a photon in either material produces an electron-hole pair, usually referred to as an *exciton* whose binding energy is of the order of about

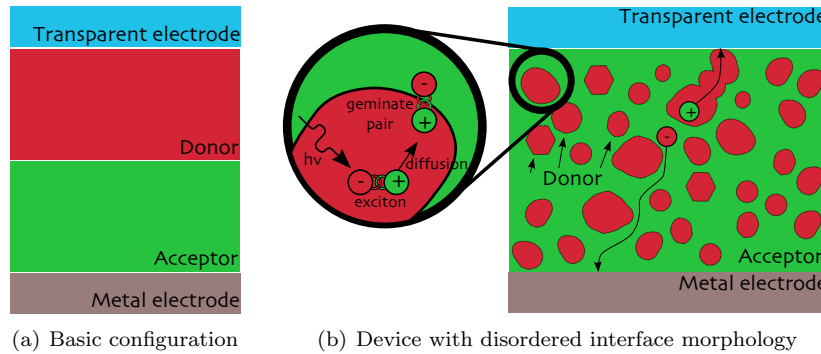


Figure 1: Structure of an organic solar cell.

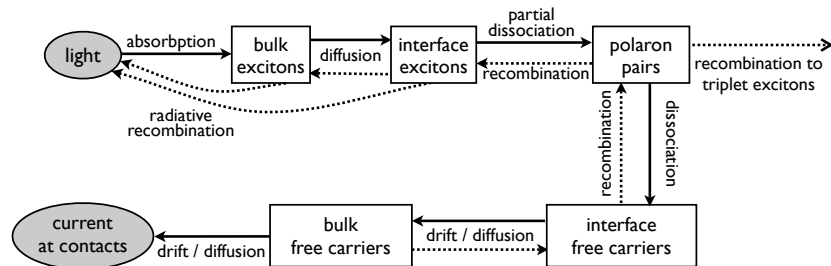


Figure 2: Flow-chart of the photoconversion mechanisms in an OSC.

0.5 ÷ 1 eV. Excitons may diffuse through the device until they either recombine or reach the interface between the donor and acceptor phases. If this latter event occurs, the exciton may get trapped at the interface in such a way that its electron component lays in the high electron affinity region while the hole component lays in the low electron affinity region. Such a trapped excited state is referred to as a *polaron pair* or *geminate pair* [3, 33] and has a lower binding energy compared to that of the exciton state, as the Coulomb attraction between the electron and hole is reduced by the chemical potential drop between the two materials. The polaron binding force may be overcome by the electric field induced by the small built-in voltage between the contact metals thus leading to the formation of two independent charged particles (one electron and one hole), otherwise the polaron pair may return to the untrapped exciton state or recombine. Free charge carriers move by drift and diffusion mechanisms and, unless they are captured along their path by the coulombic attraction of an oppositely charged particle and recombine at the interface to form a new polaron pair, they eventually reach the contacts thus producing a measurable external current.

3. Mathematical Model

In this section we propose a multiscale PDE/ODE model of photoconversion and charge transport mechanisms in an OSC which represents a consistent generalization of the approach proposed in [3, 32, 33]. To present our model we proceed through four steps. In Section 3.1, we introduce the geometrical model of the device which consist of two bulk regions (the acceptor and donor phases) separated by an interface region of (finite) thickness $2H$. In Section 3.2, we introduce the conservation laws that govern transport of the various species throughout the device and the generation and recombination mechanisms that occur in each area of the domain. In Section 3.3, we obtain the final model equations by performing an integration along the interface thickness. This leads to a mathematical description of an OSC where charge dissociation and recombination mechanisms turn out to be “lumped” into suitable transmission conditions across the surface separating the two material phases. Finally, in Section 3.4 we illustrate and discuss a model for the polaron pair dissociation rate as a function of the electric field at the material interface.

3.1. Geometry

A schematic 3D picture of the OSC is illustrated in Fig. 3(a).

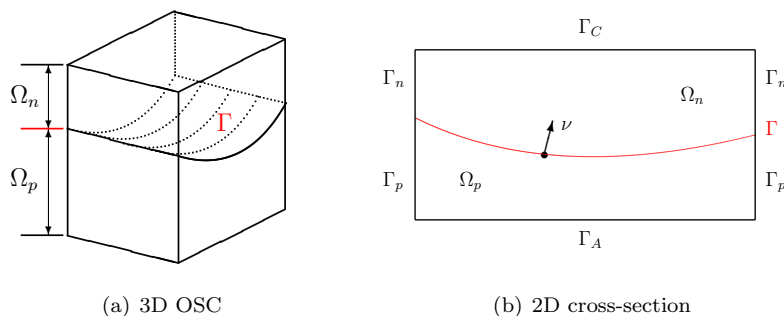


Figure 3: Geometry of the cell bulk.

The device structure Ω is a parallelepiped divided into two distinct subregions, Ω_n (acceptor) and Ω_p (donor), separated by a regular oriented surface $\Gamma = \partial\Omega_n \cap \partial\Omega_p$ [10] on which, for each $\mathbf{x} \in \Gamma$, we can define a unit normal vector $\boldsymbol{\nu}(\mathbf{x})$ directed from Ω_p into Ω_n . The top and bottom surfaces of the structure are the cell electrodes, cathode and anode, denoted as Γ_C and Γ_A , respectively, in such a way that $\partial\Omega_n = \Gamma_C \cup \Gamma \cup \Gamma_n$ and $\partial\Omega_p = \Gamma_A \cup \Gamma \cup \Gamma_p$ (see Fig. 3(b)).

Following [3, 32, 33], it is convenient, for modeling purposes, to associate with the interface Γ the subregion $\Omega_H \subset \Omega$ depicted in Fig. 4(a) and defined as follows. For each point $\mathbf{x} \in \Gamma$, let $t_{\mathbf{x}} = \{\mathbf{x} + \xi\boldsymbol{\nu}(\mathbf{x}) : |\xi| < H\}$ be the “thickness”

associated with \mathbf{x} . Then, set

$$\Omega_H = \bigcup_{\mathbf{x} \in \Gamma} t_{\mathbf{x}} = \{\mathbf{y} \in \Omega : \text{dist}(\mathbf{y}, \Gamma) < H\}. \quad (1)$$

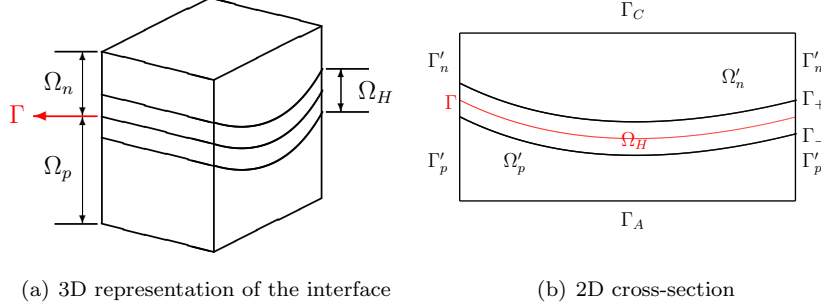


Figure 4: Geometry of the cell bulk and interface region.

The subregion Ω_H is thus a 3D thin layer of thickness $2H$ surrounding Γ and represents the device volumetric portion where the dissociation and recombination mechanisms of Section 2 are assumed to occur. Based on the definition (1), we can introduce the two portions $\Omega'_n = \Omega_n \setminus \Omega_H$ and $\Omega'_p = \Omega_p \setminus \Omega_H$, in such a way that $\Omega = \Omega'_n \cup \Omega_H \cup \Omega'_p$ (see Fig. 4(b)). Consistently, we also introduce the boundary portions Γ'_n and Γ'_p and set $\Gamma_{\pm} = \{\mathbf{x} \pm H\boldsymbol{\nu}(\mathbf{x}) : \mathbf{x} \in \Gamma\}$, in such a way that $\partial\Omega'_n = \Gamma_C \cup \Gamma_+ \cup \Gamma'_n$, $\partial\Omega'_p = \Gamma_A \cup \Gamma_- \cup \Gamma'_p$ and $\partial\Omega_H = \Gamma_+ \cup \Gamma_- \cup \Gamma_H$, where $\Gamma_H = (\Gamma_n \cup \Gamma_p) \setminus (\Gamma'_n \cup \Gamma'_p)$.

3.2. Governing Equations

Let us denote by e , n , p and P the *volumetric densities* of (singlet) excitons, electrons, holes and polaron pairs, respectively. Such quantities satisfy, for each time $t > 0$, a set of coupled conservation laws. In particular, excitons in the bulk regions obey

$$\frac{\partial e}{\partial t} + \nabla \cdot \mathbf{J}_e = Q - \frac{e}{\tau_e} \quad \text{in } \Omega'_n \cup \Omega'_p \quad (2a)$$

\mathbf{J}_e and τ_e being the exciton *flux density* and *lifetime*, respectively. The term Q in (2a) denotes the rate at which excitons are generated by photon absorption and is henceforth assumed to be a given function of time and position. In the interface region additional dissociation and recombination mechanisms must be taken into account, therefore the conservation equation for excitons in such region reads

$$\frac{\partial e}{\partial t} + \nabla \cdot \mathbf{J}_e = Q - \frac{e}{\tau_e} - \frac{e}{\tau_{diss}} + \eta k_{rec} P \quad \text{in } \Omega_H \quad (2b)$$

where τ_{diss}^{-1} is the rate at which excitons transition to the polaron state, while ηk_{rec} is the rate at which polarons transition back to the exciton state. In particular k_{rec} denotes the total rate of polaron recombination events and $0 < \eta \leq 1$ the fraction of such events which produce a singlet exciton. Finally, as excitons have zero net charge, their flux is driven by diffusion forces only, *i.e.* the flux density may be expressed as

$$\mathbf{J}_e = -D_e \nabla e \quad \text{in } \Omega \quad (2c)$$

D_e being the *exciton diffusion coefficient*.

As we assume that electrons (holes) are not able to penetrate the donor (acceptor) material beyond the interface layer Ω_H , the following equations hold for electrons in the bulk:

$$\begin{cases} \frac{\partial n}{\partial t} - \frac{1}{q} \nabla \cdot \mathbf{J}_n = 0 & \text{in } \Omega'_n \\ n \equiv 0 & \text{in } \Omega'_p \end{cases} \quad (3a)$$

and for holes in the bulk:

$$\begin{cases} p \equiv 0 & \text{in } \Omega'_n \\ \frac{\partial p}{\partial t} + \frac{1}{q} \nabla \cdot \mathbf{J}_p = 0 & \text{in } \Omega'_p \end{cases} \quad (3b)$$

where \mathbf{J}_n (\mathbf{J}_p) denotes the electron (hole) *current density* and q is the *quantum of charge*. Notice that the right-hand-side of (3a)₁ and (3b)₂ are both identically zero as electrons and holes can only recombine with each other, so no recombination occurs where either of the two species is missing. In the interface region both electrons and holes exist so the current continuity equations in such region read

$$\frac{\partial n}{\partial t} - \frac{1}{q} \nabla \cdot \mathbf{J}_n = k_{diss} P - \gamma np \quad \text{in } \Omega_H \quad (3c)$$

and

$$\frac{\partial p}{\partial t} + \frac{1}{q} \nabla \cdot \mathbf{J}_p = k_{diss} P - \gamma np \quad \text{in } \Omega_H, \quad (3d)$$

where k_{diss} is the *polaron dissociation rate* (see Section 3.4 for the model) and γ is the *bimolecular recombination rate*, for which a Langevin-type relation is used [3]. As electrons and holes each bear a non-zero net charge, their flux is driven by both diffusion and electric drift forces [19], therefore:

$$\begin{cases} \mathbf{J}_n = q(D_n \nabla n + \mu_n n \mathbf{E}) & \text{in } \Omega'_n \cup \Omega_H \\ \mathbf{J}_p = q(-D_p \nabla p + \mu_p p \mathbf{E}) & \text{in } \Omega'_p \cup \Omega_H \end{cases} \quad (3e)$$

where D_n , μ_n and D_p , μ_p are the *diffusion coefficient* and *mobility* for electrons and holes, respectively, that are assumed to satisfy the Einstein relations

$$D_n = (K_b T / q) \mu_n, \quad D_p = (K_b T / q) \mu_p \quad (3f)$$

K_b and T being Boltzmann's constant and absolute temperature, respectively. Neglecting the effect of energetic disorder, as in [3], mobilities can be assumed to depend only on the electric field magnitude, according to the Poole-Frenkel model [14, 18].

The *electric field* \mathbf{E} in (3e) is connected by

$$\mathbf{E} = -\nabla\varphi \quad \text{in } \Omega \quad (4a)$$

to the *electric potential* φ , which in turn satisfies the following Poisson equation in the two bulk regions:

$$\begin{cases} -\nabla \cdot (\varepsilon \nabla \varphi) = -qn & \text{in } \Omega'_n \\ -\nabla \cdot (\varepsilon \nabla \varphi) = +qp & \text{in } \Omega'_p \end{cases} \quad (4b)$$

while in the interface region we have

$$-\nabla \cdot (\varepsilon \nabla \varphi) = q(p - n) \quad \text{in } \Omega_H. \quad (4c)$$

The *electric permittivity* $\varepsilon = \varepsilon_r \varepsilon_0$, ε_r and ε_0 being the relative material and vacuum permittivities, respectively, is assumed constant in each material but may be discontinuous across the interface Γ .

As for the polarons, they only exist in the interface region where they are trapped in and are not allowed to move, therefore they satisfy the following ODE in the interface region

$$\frac{\partial P}{\partial t} = \frac{e}{\tau_{diss}} + \gamma np - (k_{diss} + k_{rec})P \quad \text{in } \Omega_H \quad (5a)$$

while their density is identically zero in the bulk

$$P \equiv 0 \quad \text{in } \Omega'_n \cup \Omega'_p. \quad (5b)$$

3.3. Lumping of the Interface Equations

The equation system (2)-(5) constitutes a full model of photocurrent generation in an heterojunction OSC. The domain partitioning required by such model, though, may turn out to be quite unpractical for numerical simulation, in particular when devices with complex interface morphology are to be considered. For this reason, we proceed in this section to a modification of the model which, at the cost of a few physically reasonable approximations, allows us to get rid of all equations set in the domain Ω_H by replacing them with suitable interface conditions to be enforced on the surface Γ itself. Mathematically, this procedure consists of neglecting the thickness H of the physical interface region in the ‘‘bulk’’ equations (2a), (3a), (3b), (4b) and integrating the ‘‘interface’’ equations (2b), (3c), (3d), (4c), (5a) along the direction normal to the surface Γ . With this aim, let us start by introducing the following new dependent variable

$$\tilde{P}(t, \mathbf{x}) = \int_{-H}^H P(t, \mathbf{x} + \xi \boldsymbol{\nu}(\mathbf{x})) d\xi, \quad \mathbf{x} \in \Gamma. \quad (6)$$

This quantity physically represents the *areal concentration* of polaron pairs over the surface Γ . We can derive from (5a) an evolution equation for \tilde{P} as follows:

$$\begin{aligned} \frac{\partial}{\partial t} \tilde{P}(t, \mathbf{x}) &= \int_{-H}^H \frac{1}{\tau_{diss}} e(t, \mathbf{x} + \xi \boldsymbol{\nu}(\mathbf{x})) d\xi \\ &+ \int_{-H}^H \gamma n(t, \mathbf{x} + \xi \boldsymbol{\nu}(\mathbf{x})) p(t, \mathbf{x} + \xi \boldsymbol{\nu}(\mathbf{x})) d\xi \\ &- \int_{-H}^H (k_{diss} + k_{rec}) P(t, \mathbf{x} + \xi \boldsymbol{\nu}(\mathbf{x})) d\xi. \end{aligned} \quad (7)$$

Eq. (7) may be simplified using the approximations:

$$\int_{-H}^H \frac{1}{\tau_{diss}} e(t, \mathbf{x} + \xi \boldsymbol{\nu}(\mathbf{x})) d\xi \simeq \frac{2H}{\tau_{diss}} e(t, \mathbf{x}) \quad (8a)$$

$$\int_{-H}^H \gamma n(t, \mathbf{x} + \xi \boldsymbol{\nu}(\mathbf{x})) p(t, \mathbf{x} + \xi \boldsymbol{\nu}(\mathbf{x})) d\xi \simeq 2H \gamma n(t, \mathbf{x}) p(t, \mathbf{x}) \quad (8b)$$

$$\int_{-H}^H k_{rec} P(t, \mathbf{x} + \xi \boldsymbol{\nu}(\mathbf{x})) d\xi \simeq k_{rec} \tilde{P}(t, \mathbf{x}) \quad (8c)$$

$$\int_{-H}^H k_{diss} P(t, \mathbf{x} + \xi \boldsymbol{\nu}(\mathbf{x})) d\xi \simeq k_{diss} \tilde{P}(t, \mathbf{x}) \quad (8d)$$

which lead to the following equation for the areal polaron density

$$\frac{\partial \tilde{P}}{\partial t} = \frac{2H}{\tau_{diss}} e + 2H \gamma n p - (k_{diss} + k_{rec}) \tilde{P} \quad \text{on } \Gamma. \quad (9)$$

In what follows, for any function $f : \Omega \rightarrow \mathbb{R}$, we indicate by f_n and f_p the restrictions of f on Γ from the acceptor and donor sides of the interface, and denote by $\llbracket f \rrbracket := f_n - f_p$ the *jump* of f across Γ .

Neglecting the thickness of the interface region in (2a) we obtain

$$\frac{\partial e}{\partial t} + \nabla \cdot \mathbf{J}_e = Q - \frac{e}{\tau_e} \quad \text{in } \Omega \setminus \Gamma. \quad (10)$$

Integrating (2b) across the thickness H and using again (8a) and (8c), we get

$$\int_{-H}^H \left(\frac{\partial e}{\partial t} + \nabla \cdot \mathbf{J}_e - Q + \frac{e}{\tau_e} \right) d\xi = \eta k_{rec} \tilde{P} - \frac{2H}{\tau_{diss}} e. \quad (11)$$

In order to simplify the integral in (11), we let $0 < \delta < H$ and $\forall \mathbf{x} \in \Gamma$ we make use of the following splitting

$$\int_{-H}^H = \int_{-H}^{-\delta} + \int_{-\delta}^{\delta} + \int_{\delta}^H. \quad (12)$$

The first and third term in the splitting are identically zero due to (10), while, as $\delta \rightarrow 0$,

$$\int_{-\delta}^{\delta} \left(\frac{\partial e}{\partial t} - Q + \frac{e}{\tau_e} \right) d\xi \rightarrow 0$$

and

$$\int_{-\delta}^{\delta} \nabla \cdot \mathbf{J}_e d\xi = +\boldsymbol{\nu}(\mathbf{x}) \cdot \mathbf{J}_e(t, \mathbf{x} + \delta \boldsymbol{\nu}(\mathbf{x})) - \boldsymbol{\nu}(\mathbf{x}) \cdot \mathbf{J}_e(t, \mathbf{x} - \delta \boldsymbol{\nu}(\mathbf{x}))$$

so that, using (12) in (11) and letting $\delta \rightarrow 0$ yields

$$\llbracket \boldsymbol{\nu} \cdot \mathbf{J}_e \rrbracket = \eta k_{rec} \tilde{P} - \frac{2H}{\tau_{diss}} e \quad \text{on } \Gamma. \quad (13)$$

A similar procedure may be applied to the continuity equations (3). We first rewrite (3a) and (3b) neglecting the thickness of Ω_H , obtaining:

$$\begin{cases} \frac{\partial n}{\partial t} - \frac{1}{q} \nabla \cdot \mathbf{J}_n = 0 & \text{in } \Omega_n \\ n \equiv 0 & \text{in } \Omega_p \end{cases} \quad (14)$$

and

$$\begin{cases} p \equiv 0 & \text{in } \Omega_n \\ \frac{\partial p}{\partial t} + \frac{1}{q} \nabla \cdot \mathbf{J}_p = 0 & \text{in } \Omega_p. \end{cases} \quad (15)$$

Then, by integrating (3c) and (3d) across the thickness H , using the splitting (12), the approximation (8b) and (8d) we end up with

$$\frac{1}{q} \boldsymbol{\nu} \cdot \mathbf{J}_p = \frac{1}{q} \boldsymbol{\nu} \cdot \mathbf{J}_n = -k_{diss} \tilde{P} + 2H \gamma n p \quad \text{on } \Gamma. \quad (16)$$

The same averaging technique as above can be used to treat the Poisson equation (4b) and (4c).

This completes the derivation of the multiscale version of the governing equations of the OSC model which, for sake of convenience, we summarize below dropping from now on the superscript \sim from the variable \tilde{P} :

$$\frac{\partial P}{\partial t} = \frac{2H}{\tau_{diss}} e + 2H\gamma np - (k_{diss} + k_{rec})P \quad \text{on } \Gamma, \quad (17a)$$

$$\begin{cases} \frac{\partial e}{\partial t} - \nabla \cdot (D_e \nabla e) = Q - \frac{e}{\tau_e} & \text{in } \Omega_n \cup \Omega_p \equiv \Omega \setminus \Gamma \\ \llbracket e \rrbracket = 0, \quad \llbracket -\boldsymbol{\nu} \cdot D_e \nabla e \rrbracket = \eta k_{rec} P - \frac{2H}{\tau_{diss}} e & \text{on } \Gamma, \end{cases} \quad (17b)$$

$$\begin{cases} \frac{\partial n}{\partial t} - \nabla \cdot (D_n \nabla n - \mu_n n \nabla \varphi) = 0 & \text{in } \Omega_n \\ \boldsymbol{\nu} \cdot (D_n \nabla n - \mu_n n \nabla \varphi) = -k_{diss} P + 2H\gamma np & \text{on } \Gamma, \end{cases} \quad (17c)$$

$$\begin{cases} \frac{\partial p}{\partial t} - \nabla \cdot (D_p \nabla p + \mu_p p \nabla \varphi) = 0 & \text{in } \Omega_p \\ -\boldsymbol{\nu} \cdot (D_p \nabla p + \mu_p p \nabla \varphi) = -k_{diss} P + 2H\gamma np & \text{on } \Gamma, \end{cases} \quad (17d)$$

$$\begin{cases} -\nabla \cdot (\varepsilon \nabla \varphi) = -qn & \text{in } \Omega_n \\ -\nabla \cdot (\varepsilon \nabla \varphi) = +qp & \text{in } \Omega_p \\ \llbracket \varphi \rrbracket = \llbracket \boldsymbol{\nu} \cdot \varepsilon \nabla \varphi \rrbracket = 0 & \text{on } \Gamma. \end{cases} \quad (17e)$$

Eqs. (17) must be supplemented by appropriate boundary conditions and initial data for e , n , p and P . Referring to [12] and [32] for the physical details, we merely notice that Dirichlet boundary conditions are enforced for e and φ on Γ_C and Γ_A , Robin-type conditions are given for n and p on Γ_C and Γ_A , respectively, while homogeneous Neumann conditions are assumed on the remaining boundary $\Gamma_n \cup \Gamma_p$.

3.4. Model for the Polaron Dissociation Rate

We devote this section to describing the model for the polaron dissociation rate k_{diss} as a function of the electric field at the material interface, since this parameter turns out to have a significant impact on the cell photoconversion efficiency as documented in Section 5.

Referring to Fig. 5 for the geometrical notation, we let

$$k_{diss}(\mathbf{E}) = k_{diss}(0) \int_0^{2\pi} d\psi \int_0^{\pi/2} w(\theta, \psi) \beta(\mathbf{E} \cdot \mathbf{v}) d\theta, \quad (18)$$

where $k_{diss}(0)$ is the zero-field dissociation rate constant, \mathbf{v} is the escape direction of the electron part of the polaron at the point $\mathbf{x} \in \Gamma$, w is a nonnegative weight such that $\int_0^{2\pi} d\psi \int_0^{\pi/2} w(\theta, \psi) d\theta = 1$, and β is an enhancement/suppression factor given by the Poole-Frenkel formula

$$\beta(z) = \begin{cases} e^{-Az} & z \geq 0 \\ e^{2\sqrt{-Az}} & z < 0, \end{cases} \quad (19)$$

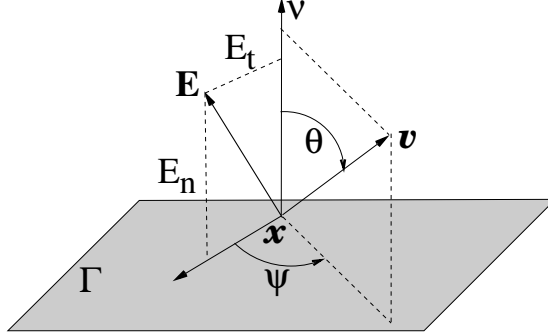


Figure 5: Polaron dissociation at the material interface.

having set $A = (4\pi\epsilon)^{-1}q^3(K_b T)^{-2}$. The product $\mathbf{E} \cdot \mathbf{v}$ can be expressed in terms of the normal component E_n and the tangential component E_t of the electric field as

$$\mathbf{E} \cdot \mathbf{v} = E_n \cos \theta + E_t \sin \theta \cos \psi.$$

Upon assuming that \mathbf{v} forms a maximum angle θ_{max} with $\boldsymbol{\nu}$, the weight w can be expressed as:

$$w(\theta, \psi) = \begin{cases} \frac{\sin \theta}{2\pi(1 - \cos \theta_{max})} & 0 < \theta \leq \theta_{max} \\ 0 & \theta_{max} < \theta \leq \frac{\pi}{2}. \end{cases}$$

Two limits are of particular interest, $\theta_{max} = \pi/2$ and $\theta_{max} \rightarrow 0^+$. In the first case, Eq. (18) becomes

$$k_{diss}(\mathbf{E}) = k_{diss}(0) \int_0^{2\pi} d\psi \int_0^{\pi/2} \frac{\sin \theta}{2\pi} \beta(\mathbf{E} \cdot \mathbf{v}) d\theta, \quad (20)$$

which, in the special case where $E_t = 0$, coincides with Eqs. (17)-(21) of [3]. In the second case, it can be checked that

$$k_{diss}(\mathbf{E}) = k_{diss}(0) \beta(E_n). \quad (21)$$

Fig. 6 shows the dissociation rate constant (normalized to $k_{diss}(0)$) computed by model (20) (left) and (21) (right) for several values of the angle between \mathbf{E} and $\boldsymbol{\nu}$ and having set $T = 300$ K and $\epsilon_r = 4$. We notice that the dissociation rate computed by model (20) has a significantly smaller range of variability than predicted by model (21). If the electric field lies in the tangent plane at point \mathbf{x} of Γ (angle = 90° , $E_n = 0$), the resulting curve from model (20) is an even function of E_t , similarly to what predicted by classical Onsager's dissociation theory [28, 5], while in the case of model (21) the normalized dissociation does not depend on the electric field because $\beta(E_n) = 1$. A discussion of the impact of (20) and (21) on the model predictions will be carried out in Section 5.

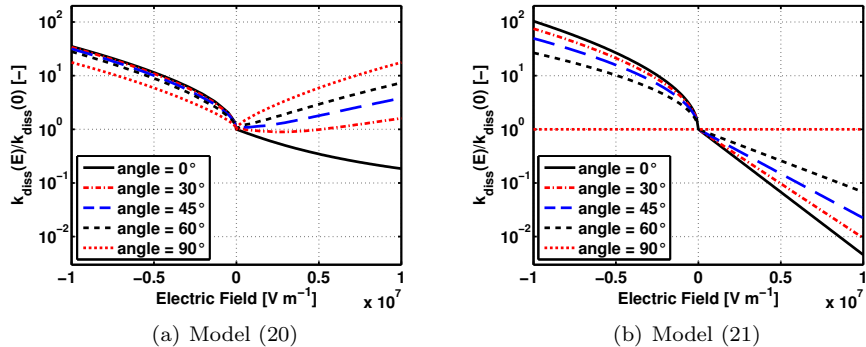


Figure 6: Comparison between models (20) and (21) for various angles between \mathbf{E} and $\boldsymbol{\nu}$.

4. Numerical Approximation

In this section we describe the numerical techniques used to solve the mathematical model introduced in Section 3.3. As the focus of the computational simulations illustrated in Section 5 is on the steady state analysis of heterojunction cell performance, we drop out all partial derivatives with respect to time t in system (17) in such a way that Eq. (9) reduces to an algebraic constraint. Should the simulation of the model in the transient regime be of future interest, it is straightforward to adapt to the case at hand the numerical method described in [12] based on Rothe's method and on the use of adaptive Backward Differencing Formulas.

The numerical strategy adopted in the present paper is basically composed of three steps:

1. Linearization
2. Spatial discretization
3. Solution of the linear algebraic system

Step (1)

For model linearization, we adopt a quasi-Newton approach similar to that used in [12] that can be described as follows. Denote by $\mathbf{U} = [\varphi, n, p, e, P]^T$ the *state vector* and introduce the nonlinear operator \mathbf{F} defined by

$$\mathbf{F}(\mathbf{U}) = [F_\varphi(\mathbf{U}), F_n(\mathbf{U}), F_p(\mathbf{U}), F_e(\mathbf{U}), F_P(\mathbf{U})]^T$$

where the i -th element of \mathbf{F} is the nonlinear (differential) operator associated with the i -th equation of system (17). Given $\mathbf{U}^{(0)}$, the k -th step of the Newton iterative method can be written as:

- *Step (1)*₁

$$\begin{aligned} &\text{Compute } \delta\mathbf{U}^{(k)} \text{ by solving} \\ &J(\mathbf{U}^{(k)})\delta\mathbf{U}^{(k)} = -\mathbf{F}(\mathbf{U}^{(k)}) \end{aligned} \quad (22)$$

- *Step (1)₂*

$$\begin{aligned} &\text{Update } \mathbf{U}^{(k)} \text{ to } \mathbf{U}^{(k+1)} \text{ by} \\ &\mathbf{U}^{(k+1)} = \mathbf{U}^{(k)} + \delta\mathbf{U}^{(k)} \end{aligned} \tag{23}$$

where $J(\mathbf{U}) = [j_{mn}(\mathbf{U})]$ denotes the Jacobian matrix of $\mathbf{F}(\mathbf{U})$ and each of its entries $j_{mn}(\mathbf{U})$ is given by the Frechét derivative of the m -th entry of \mathbf{F} with respect to the n -th entry of \mathbf{U} . As the computation of all the derivatives in $J(\mathbf{U})$ may get quite cumbersome if the electric field dependent models for the mobilities, dissociation and recombination coefficients introduced in Section 3 are used, we modify *Step (1)₁* by replacing $J(\mathbf{U})$ with an approximate Jacobian $\tilde{J}(\mathbf{U})$ in which the derivatives of the model coefficients with respect to the state vector are neglected. Possible ill-conditioning of \tilde{J} can be avoided by a proper choice of adimensionalization coefficients (see, *e.g.*, [24, 19]).

Step (2)

Similarly to [12], for the spatial discretization of the sequence of linear systems of PDEs stemming from *Step (1)* we adopt the Galerkin-Finite Element Method (G-FEM) stabilized by means on an Exponential Fitting technique [2, 13, 34, 23] in order to deal with possibly dominating drift terms in the continuity equations. A peculiarity of the heterojunction model (17) as compared to the *homogenized* model of [12] is the presence of non-trivial interface conditions at the donor-acceptor interface, which are taken care of by means of the *substructuring* techniques described, *e.g.*, in [30] which turn out to be of straightforward implementation in the adopted G-FEM method.

Step (3)

Unlike the framework of Domain Decomposition Methods, where substructuring is usually implemented by means of subdomain iterations [30], our choice here is to solve the linear algebraic systems by means of direct methods. Although this approach has proven faster and more robust in the 1- and 2D cases we have considered thus far, it may be necessary to abandon it for large 3D problems where memory consumption becomes the stronger constraint.

5. Simulation Results

In this section we carry out a validation of the model proposed in Section 3.3 by comparison with available results in the literature, showing the effectiveness of our approach in the case of complex internal morphologies without the need of particular meshing techniques. We also investigate the impact of the model for the polaron pair dissociation rate proposed in Section 3.4 on the simulated device performance. We consider a device made of F8BT and PFB, acting as acceptor and donor material respectively, as previously considered in [32, 33, 9] to which we refer for all the details about material parameters and data. The numerical schemes of Section 4 have been implemented in `Octave` using the Octave-Forge package `bim` [11] for matrix assembly.

5.1. Model Validation through Comparison with Existing Simulation Data

In this section, we aim to compare the predictions of our model to those of [32, 33]. The device morphology, shown in Figure 7, is an interpenetrating rod-shaped structure of donor and acceptor materials with $L_{cell} = 150$ nm, $L_{elec} = 50$ nm, $L_R = 79$ nm and $W_R = 6.25$ nm. Throughout this section, we denote by y the direction between the two electrodes Γ_C and Γ_A .

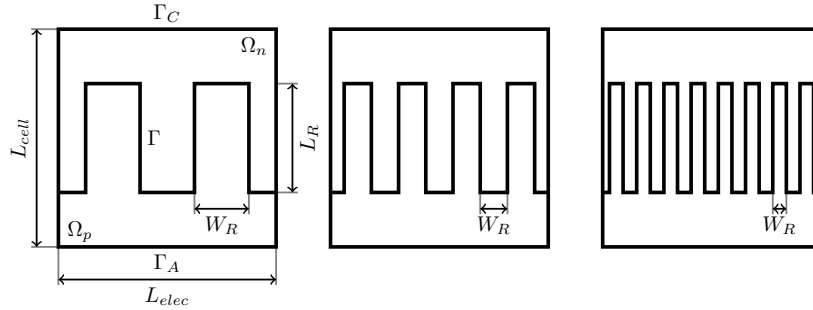


Figure 7: Internal morphology with rod-shaped donor-acceptor interface.

In [32, 33] an optical model has been used to determine the exciton generation term Q . Here, instead, we follow a simpler approach by considering Q to be constant in the entire device structure and equal to the value obtained averaging the result in [32, 33]. Moreover, simplified Dirichlet boundary conditions are enforced on the free carrier densities at the device electrodes, which amounts to neglecting the dependence of charge injection on the electric field.

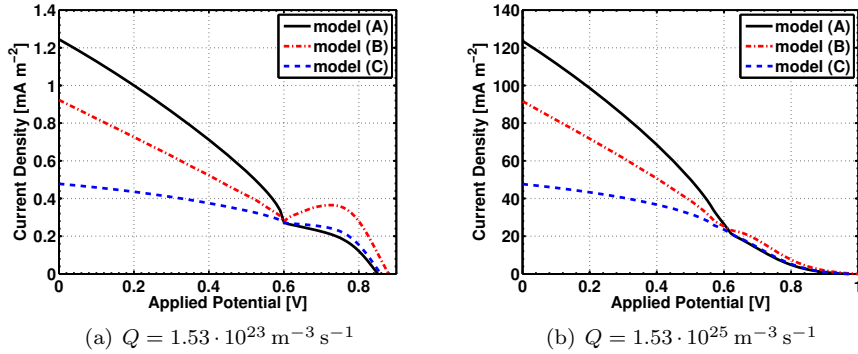


Figure 8: Comparison of the current-voltage characteristic lines with two different values for the exciton generation rate.

Figure 8(a) shows the current density-voltage characteristics in the case of an exciton generation rate $Q = 1.53 \cdot 10^{23} \text{ m}^{-3} \text{ s}^{-1}$. The three curves correspond to the use of three different expressions for the polaron dissociation rate k_{diss} ,

identified as follows: (A) the model proposed in [32, 33] with $\bar{E}_y = |\Gamma|^{-1} \int_{\Gamma} E_y dx$ as the driving parameter for polaron pair dissociation (solid line); (B) the model (20) (dash-dotted line); (C) the model (21) (dashed line). The result computed using model (A) is in excellent agreement with that of Figure 7(right) in [33] despite the above mentioned modeling differences. Model (A) does not account for the orientation of the electric field with respect to the donor-acceptor interface and is expected to overestimate dissociation in the case where $\mathbf{E} \cdot \boldsymbol{\nu} \simeq 0$. This is confirmed by the curve for model (B). As a matter of fact, in this case all the dissociation directions are assumed to be equally likely and the computed output current density before flat-band condition occurs ($V_{appl} \leq 0.6$ V) is smaller than predicted by the solid line curve. For $V_{appl} > 0.6$ V a non-monotonic behavior is observed, this most probably to be ascribed to a too important contribution of the tangential component of the electric field E_t that still leads (20) to overestimate polaron dissociation at the material interface. If, instead, model (C) is used, the obtained output current density characteristics is the dashed line in Figure 8(a). We observe a smoother trend than in previous cases for all applied voltages, and close to short circuit condition we note that the current density is further reduced since dissociation is assumed to occur only in the normal direction and on a significant portion of the interface E_n is almost vanishing. In all the considered cases, the nonsmooth behavior at flat band conditions ($V_{appl} = 0.6$ V) is to be ascribed to the discontinuity of $\partial\beta/\partial z$ at $z = 0$ in (19).

Figure 8(b) shows the results of the same analysis as above in the case of an exciton generation rate $Q = 1.53 \cdot 10^{25} \text{ m}^{-3} \text{ s}^{-1}$. The shape of the characteristics is very similar to those with low light up to a scaling factor of about 100, this suggesting a linearity between the output current density and the illumination intensity. Notice the absence of the bump for $V_{appl} > 0.6$ V in the case of model (B). This is a consequence of the increased magnitude of the charge carrier densities compared to the previously considered illumination that in turn determines stronger Coulomb attraction forces and hence more recombination phenomena. With reduced attractions, instead, charge carriers have more chances to escape from the interface following concentration gradients.

In Figure 9 we show the charge carrier densities in a device with geometrical data set to $L_{cell} = 150$ nm, $L_{elec} = 440$ nm, $L_R = 79$ nm and $W_R = 55$ nm, at short circuit condition with exciton generation rate $Q = 1.53 \cdot 10^{25} \text{ m}^{-3} \text{ s}^{-1}$. We first observe that computed charge carrier distributions in Figure 9(left) are in very good agreement with those of Figure 3(i) in [32] except near the electrodes where different boundary conditions are applied, and show the same peaks close to the vertical sides of the donor-acceptor interface. It is interesting to notice that the total number of holes in the donor material is higher than the number of electrons in the acceptor material because of the significantly different values of their respective mobilities. Negative charges can move through the device faster to be finally extracted at the cathode so that an overall positive charge builds-up in the device. The charge densities computed using models (B) and (C) exhibit a qualitatively similar profile with a gradual reduction of the magnitude

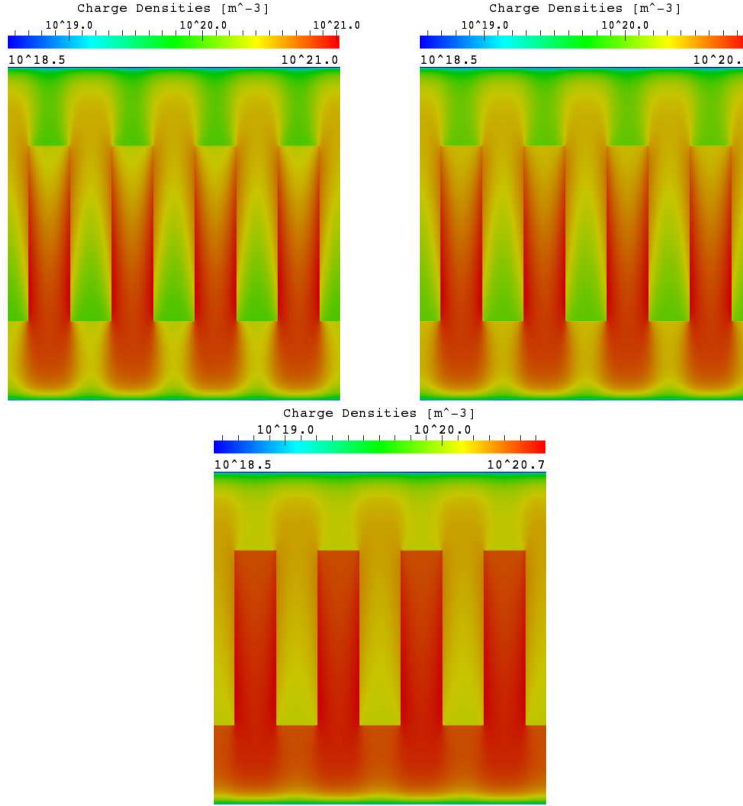


Figure 9: Charge carrier densities $[\text{m}^{-3}]$ at short circuit condition with $Q = 1.53 \cdot 10^{25} \text{ m}^{-3} \text{ s}^{-1}$ using models (A) (left), (B) (right) and (C) (bottom), respectively.

compared to the result of model (A). This behavior is completely consistent with the previous analysis of the current-voltage characteristics predicted by the three models of k_{diss} .

We conclude this preliminary validation of model (17) by illustrating in Figure 10 the open circuit voltage V_{oc} and short circuit current density J_{sc} of a device with the same characteristics as in the previous set of simulations for values of exciton generation rate in the range from $1.53 \cdot 10^{20}$ to $1.53 \cdot 10^{30} \text{ m}^{-3} \text{ s}^{-1}$. Figure 10(a) is in excellent agreement with Figure 6(right) of [33], and indicates that models (A), (B) and (C) predict a linear behavior of V_{oc} with respect to the logarithm of the exciton generation rate, as already pointed out in [32, 33]. Figure 10(b) illustrates the current density J_{sc} that can be extracted from the device at short circuit condition. The log-scale plot indicates that J_{sc} increases linearly in a wide range of illumination regimes until values of the order of $10^{28} \text{ m}^{-3} \text{ s}^{-1}$. With more intense irradiation the increase becomes sublinear,

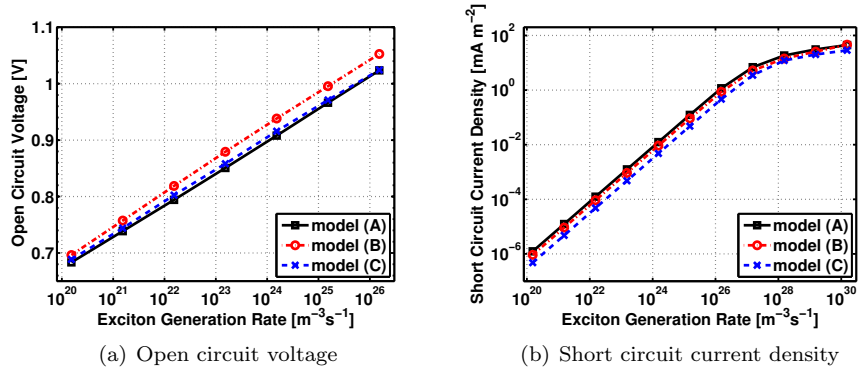


Figure 10: Open circuit voltage and short circuit current density as functions of the exciton generation rate.

suggesting that saturation of the device occurs due to more relevant excitonic and electron-hole recombination phenomena which in turn are a consequence of the increased densities.

5.2. The Role of Interface Morphology

In this section, we aim to investigate the role of interface configuration in affecting the OSC performance. Referring to Figure 7, we set $L_{cell} = L_{elec} = 150$ nm and $L_R = 75$ nm, and we analyze the importance of interfacial length by considering devices with an increasing density of interpenetrating structures, starting from a biplanar device and then taking decreasing values for the rod width W_R . Model parameters are the same as in the previous simulations and the exciton generation rate is $Q = 1.53 \cdot 10^{25} \text{ m}^{-3} \text{ s}^{-1}$.

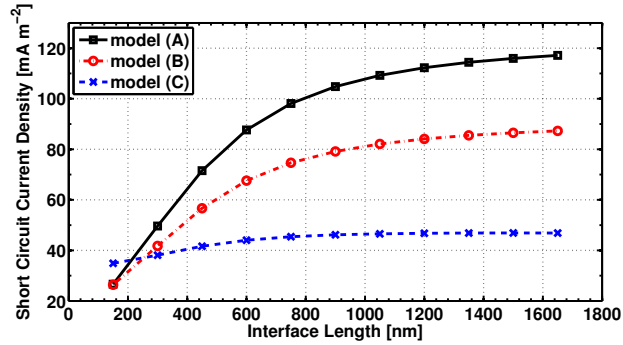


Figure 11: Short circuit current density as a function of interface length.

Figure 11 illustrates the computed short circuit current density as a function of the interfacial length for the various polaron pair dissociation rate models

we previously considered in this section. In all cases, current saturation is predicted for high densities of nanostructures due to the depletion of excitons in the interface area that in turn is a consequence of the abundance of dissociation sites. Computed saturation levels greatly differ among the three choices of the model for k_{diss} , in accordance with the analysis of Section 5.1. Figure 11 also shows that when a biplanar device is considered, using model (C) a higher short circuit current density is obtained compared to the other approaches. An explanation of this result is that the electric field in this case is actually vertically directed and this fact, combined with the assumption that dissociation occurs only in the normal direction, brings to overestimate its rate (cf. the solid lines in Figure 6). Qualitatively similar results have been obtained in [6, 32, 33].

Also the orientation of the interface is expected to play a role in determining device operation and the following set of simulations aims to investigate this issue. This is a distinctive feature of our model that, to our knowledge, has not been treated in previous works. For a proper analysis, we allow the orientation of the donor-acceptor interface to change while its overall length remains almost constant, in order to single out the effect of the former and analyze it.

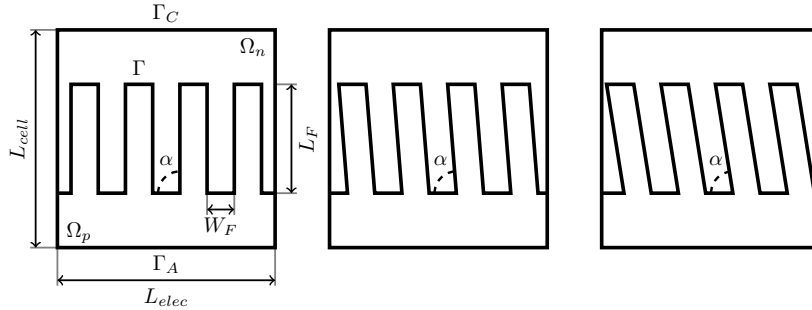


Figure 12: Internal morphology with nanorods with a varying incidence angle α .

The considered device geometry is shown in Figure 12, where the number of rods is kept constant to four for each material but the incidence angle α is varied in a range from 90° to $77^\circ 11'$. The geometric data are $L_{cell} = L_{elec} = 150$ nm, $L_R = 75$ nm and $W_R = 37.5$ nm.

Since the changes in the amplitude for α are small, the interface length does not vary significantly (as demonstrated by Figure 13(a)) and we expect model (A) to be quite insensitive to such small modifications since E_y mainly depends on the potential drop across the electrodes. Concerning with model (B), we again do not expect a relevant sensitivity to such variations in the interface morphology since the changes in E_n and E_t should balance in the overall contribution. We instead expect model (C) to be most sensitive since the normal field that is screened at the interface may experience significant variations as a function of the angle α .

Our expectations are confirmed by the results in Figure 13(b), showing that

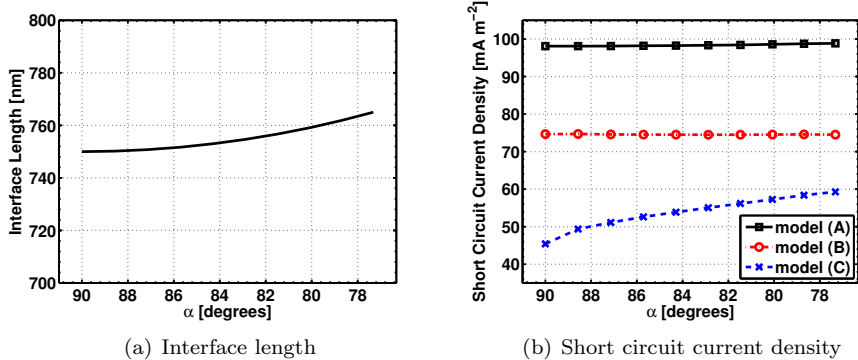


Figure 13: Interface length and short circuit current density as functions of α .

the performance of the device in terms of computed short circuit current density does not vary with α when models (A) and (B) are considered, while if model (C) is used, an increase of the short circuit current density is observed as soon as the inclination of the nanorod structure is modified with respect to the initial configuration. This behavior can be explained as follows. The choice of model (21) predicts an increase of the dissociation for negative values of the normal electric field that is higher than the reduction for positive values of E_n . Since at short circuit the electric field can be reasonably assumed to be directed along the y axis (*i.e.*, from the cathode to the anode), the sides of each rod experience opposite normal fields. As a result, the overall effect is dominated by the contribution of the sides with negative fields and dissociation is enhanced.

5.3. The Case of A Complex Interface Morphology

In this concluding section, we test the versatility of the model proposed in the present article in dealing with a very complex internal morphology as that shown in Figure 14. In this regard, it is important to notice that the use of the full-scale model (2)-(5) would require an extremely fine grid resolution to accurately describe the volumetric terms in the active layer around the donor-acceptor interface, while the use of the multiscale lumped model (17) has the twofold advantage of considerably simplifying the design of the computational mesh and reducing the size of the nonlinear algebraic system to be solved.

Figure 15(a) illustrates the computed charge carrier density at short circuit ($V_{appl} = 0$) for the geometry of Figure 14, where the domain is a square 150 nm sided, with exciton generation rate $Q = 1.53 \cdot 10^{25} \text{ m}^{-3} \text{ s}^{-1}$ and using model (B) for k_{diss} . Notice in particular that the densities assume much higher magnitudes compared to those of Figure 9. This is a consequence of the complexity of the geometry, where donor and acceptor form dead-end areas in which the charges are trapped and experience recombination. In Figure 15(b) we show again a comparison of the current-voltage characteristics obtained using the three

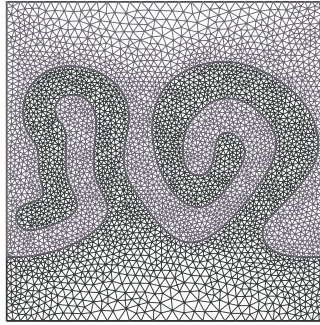


Figure 14: The computational mesh used to numerically solve the model of Section 3.3 in the case of a complex geometry.

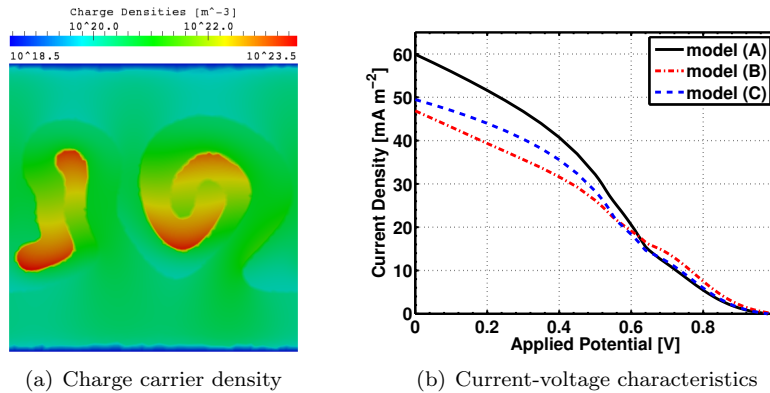


Figure 15: Log-plot of charge carrier density [m^{-3}] and current-voltage characteristics for a device with very complex internal structure.

different polaron dissociation rate models. The differences among the obtained characteristic lines are reduced with respect to the previous simulated cases. In particular the computed short circuit current densities attain closer values with respect to more regular morphologies, such as that of Figure 7, for comparable values of the interface length (approximately 900 nm), see Figure 11. This is probably to be ascribed to the tortuosity of device internal morphology which makes interface recombination effects more significant than in the case of a more regular internal structure.

6. Concluding Remarks and Future Perspectives

The research activity object of the present article is a continuation of the mathematical study of organic photovoltaic devices started off in [12], and is focused to:

- the accurate and computationally efficient modeling of the photoconversion

mechanisms occurring in the material bulk and, above all, at the material interface separating the acceptor and donor layers;

- the investigation of the impact of the interface morphology and of polaron pair dissociation on device performance.

To the purpose of achieving the above objectives, we first propose a full-scale multi-dimensional model for bilayer organic solar cell devices with arbitrary interface geometries. Then, we carry out a suitable averaging process of the mass balance system equations across the interface thickness, which amounts to “lumping” the equations describing the interface phenomena into suitable flux transmission conditions. The resulting mathematical model consists of a system of incompletely parabolic nonlinear PDEs in drift-diffusion form to describe mass transport in the materials, coupled with ODEs localized at the heterojunction.

The approach proposed here to deal with photoconversion mechanisms in heterogeneous organic solar cells, has a distinctive multiscale flavour and is similar to model-reduction techniques used in porous media with thin fractures [25]. Our formulation, compared to previously proposed multi-dimensional models [6, 33, 20], has the advantage to simplify the discrete computational domain while allowing, at the same time, to easily include in the model a local dependency of the coefficients on the orientation of the electric field.

This latter issue is thoroughly addressed in the numerical simulations of two-dimensional realistic device structures aimed to investigating the principal device design parameters (short circuit current and open circuit voltage) as functions of material interface morphology. In particular, a novel approach to consistently account for interface electric field orientation in the polaron dissociation rate is proposed and successfully compared to previously existing (simplified) expressions depending on a suitable average of the electric field.

Research topics currently under scrutiny include:

- application of the proposed computational model to the study of more complex three-dimensional morphologies, as considered in [21];
- inclusion of time dependency in the computational experiments, in order to extend to bilayer OSCs the analysis carried out in [12];
- development of an existence and well-posedness analysis of the solution of the proposed equation system (17) in both stationary and time-dependent regimes.

Future efforts will be devoted to investigating more advanced models for carrier mobilities and polaron dissociation rate, as well as to considering other material blends currently employed in the fabrication of up-to-date organic solar cells (see, *e.g.*, [1, 4, 7]).

7. Acknowledgements

The authors wish to gratefully acknowledge the contribution of Maurizio M. Cogliati to the research topic addressed in this article. They also wish to thank Dr. Dario Natali from Dipartimento di Elettronica e Informazione, Politecnico di Milano and Dr. Mosè Casalegno from Dipartimento di Chimica “Giulio Natta”, Politecnico di Milano for many fruitful and stimulating discussions. The third author was supported by the M.U.R.S.T. grant nr. 200834WK7H005 *Adattività Numerica e di Modello per Problemi alle Derivate Parziali* (2010-2012).

References

- [1] D. Bagnis, L. Beverina, H. Huang, F. Silvestri, Y. Yao, H. Yan, G.A. Pagani, T.J. Marks, and A. Facchetti, *Marked alkyl- vs alkenyl-substituent effects on squaraine dye solid-state structure, carrier mobility, and bulk-heterojunction solar cell efficiency*, Journal of the American Chemical Society **132** (2010), no. 12, 4074–4075, PMID: 20205468.
- [2] R.E. Bank, W.M. Coughran Jr, and L.C. Cowsar, *The finite volume Scharfetter-Gummel method for steady convection diffusion equations*, Computing and Visualization in Science **1** (1998), no. 3, 123–136.
- [3] J.A. Barker, C.M. Ramsdale, and N.C. Greenham, *Modeling the current-voltage characteristics of bilayer polymer photovoltaic devices*, Physical Review B **67** (2003), 075205 (9pp).
- [4] L. Beverina and P. Salice, *Squaraine compounds: Tailored design and synthesis towards a variety of material science applications*, European Journal of Organic Chemistry **2010** (2010), no. 7, 1207–1225.
- [5] C.L. Braun, *Electric field assisted dissociation of charge transfer states as a mechanism of photocarrier production*, The Journal of Chemical Physics **80** (1984), 4157.
- [6] G.A. Buxton and N. Clarke, *Computer simulation of polymer solar cells*, Modelling Simul. Mater. Sci. Eng. **15** (2007), 13–26.
- [7] M. Caironi, T. Agostinelli, D. Natali, M. Sampietro, R. Cugola, M. Catellani, and S. Luzzati, *External quantum efficiency versus charge carriers mobility in polythiophene/methanofullerene based planar photodetectors*, J. Appl. Phys. **102** (2007), no. 2, 024503–024509.
- [8] K.M. Coakley and M.D. McGehee, *Conjugated polymer photovoltaic cells*, Chemistry of Materials **16** (2004), no. 23, 4533–4542.
- [9] M.M. Cogliati and M. Porro, *Third generation solar cells: Modeling and simulation*, 2010, Master Thesis, Politecnico di Milano, <http://www1.mate.polimi.it/biblioteca/tesiview.php?id=368&L=i>.

- [10] R. Dautray and J.-L. Lions, *Mathematical analysis and numerical methods for science and technology. Functional and variational methods*, vol. 2, Springer, 1988.
- [11] C. de Falco and M. Culpò, *bim octave-forge package*, <http://octave.sourceforge.net/bim/index.html>.
- [12] C. de Falco, R. Sacco, and M. Verri, *Analytical and numerical study of photocurrent transients in organic polymer solar cells*, *Computer Methods in Applied Mechanics and Engineering* **199** (2010), no. 25-28, 1722 – 1732.
- [13] E. Gatti, S. Micheletti, and R. Sacco, *A new Galerkin framework for the drift-diffusion equation in semiconductors*, *East West Journal of Numerical Mathematics* **6** (1998), 101–136.
- [14] W.D. Gill, *Drift mobilities in amorphous charge-transfer complexes of trinitrofluorenone and poly-n-vinylcarbazole*, *J. Appl. Phys.* **55** (1972), no. 12, 5033.
- [15] S. Gunes, H. Neugebauer, and N.S. Sariciftci, *Conjugated polymer-based organic solar cells*, *Chem. Rev.* **107** (2007), 1324–1338.
- [16] J.M. Halls and R.H. Friend, *Organic photovoltaic devices*, *Clean energy from photovoltaics* (M.D. Archer and R. Hill, eds.), vol. 1, World Scientific, 2001, pp. 377–445.
- [17] Heliatek Labs, *Heliatek website*, <http://www.heliatek.com/news-19>, 11-10-2010.
- [18] G. Horowitz, *Organic field-effect transistors*, *Advanced Materials* **10** (1998), no. 5, 365–377.
- [19] J.W. Jerome, *Analysis of charge transport*, Springer-Verlag, Berlin Heidelberg, 1996.
- [20] J.W. Jerome, M.A. Ratner, J.D. Servaites, C.-W. Shu, and S. Tan, *Simulation of the buxton-clarke model for organic photovoltaic cells*, *Computational Electronics (IWCE)*, 2010 14th International Workshop on, 2010, pp. 1 –4.
- [21] R.G.E. Kimber, A.B. Walker, G.E. Schroeder-Turk, and D.J. Cleaver, *Bi-continuous minimal surface nanostructures for polymer blend solar cells*, *Phys. Chem. Chem. Phys.* **12** (2010), 844–851.
- [22] Konarka Technologies, Inc., *Konarka’s power plastic achieves world record 8.3% efficiency certification from national energy renewable laboratory (nrel)*, Press release, 2010.
- [23] R.D. Lazarov and L.T. Zikatanov, *An exponential fitting scheme for general convection-diffusion equations on tetrahedral meshes*, *Institute for Scientific Computation* **1** (2005), no. 92, 60–69.

- [24] P.A. Markowich, *The stationary semiconductor device equations*, Springer-Verlag, Wien-New York, 1986.
- [25] V. Martin, J. Jaffré, and J. E. Roberts, *Modeling fractures and barriers as interfaces for flow in porous media*, SIAM J. Sci. Comp. **26** (2005), 1667–1691.
- [26] A.C. Mayer, S.R. Scully, B.E. Hardin, M.W. Rowell, and M.D. McGehee, *Polymer-based solar cells*, Materials Today **10** (2007), no. 11, 28–33.
- [27] V.D. Mihailetschi, L.J.A. Koster, J.C. Hummelen, and P.W.M. Blom, *Photocurrent generation in polymer-fullerene bulk heterojunctions*, Physical Review Letters **93** (2004), no. 21, 216601 (4pp).
- [28] L. Onsager, *Initial recombination of ions*, Physical Review **54** (1938), no. 8, 554–557.
- [29] M. Pope, *Electronic processes in organic crystals and polymers*, Oxford University Press, Oxford Oxfordshire, 1999.
- [30] A. Quarteroni and A. Valli, *Domain decomposition methods for partial differential equations*, Numerical mathematics and scientific computation, Clarendon Press, 1999.
- [31] C.W. Tang, *Two-layer organic photovoltaic cell*, Appl. Phys. Lett. **48** (1986), 183.
- [32] J. Williams, *Finite element simulations of excitonic solar cells and organic light emitting diodes*, Ph.D. thesis, University of Bath, 2008.
- [33] J. Williams and A.B. Walker, *Two-dimensional simulations of bulk heterojunction solar cell characteristics*, Nanotechnology **19** (2008), 424011.
- [34] J. Xu and L. Zikatanov, *A monotone finite element scheme for convection-diffusion equations*, Mathematics of Computation **68** (1999), no. 228, 1429–1446.